Biophysical Journal Volume 105 November 2013 2130–2140

Molecular and Subcellular-Scale Modeling of Nucleotide Diffusion in the Cardiac Myofilament Lattice

Peter M. Kekenes-Huskey,[†*] Tao Liao,[‡] Andrew K. Gillette,[§] Johan E. Hake,[¶] Yongjie Zhang,[‡] Anushka P. Michailova,[‖] Andrew D. McCulloch,[‖] and J. Andrew McCammon[††]

[†]Department of Pharmacology and [§]Department of Mathematics, University of Arizona, California; [¶]Simula School of Research and Innovation, Oslo, Norway; and [‡]Department of Mechanical Engineering, Carnegie Mellon University, Pittsburgh, Pennsylvania; [‖]Department of Bioengineering and [††]Howard Hughes Medical Institute, University of California, San Diego, California

ABSTRACT Contractile function of cardiac cells is driven by the sliding displacement of myofilaments powered by the cycling myosin crossbridges. Critical to this process is the availability of ATP, which myosin hydrolyzes during the cross-bridge cycle. The diffusion of adenine nucleotides through the myofilament lattice has been shown to be anisotropic, with slower radial diffusion perpendicular to the filament axis relative to parallel, and is attributed to the periodic hexagonal arrangement of the thin (actin) and thick (myosin) filaments. We investigated whether atomistic-resolution details of myofilament proteins can refine coarse-grain estimates of diffusional anisotropy for adenine nucleotides in the cardiac myofibril, using homogenization theory and atomistic thin filament models from the Protein Data Bank. Our results demonstrate considerable anisotropy in ATP and ADP diffusion constants that is consistent with experimental measurements and dependent on lattice spacing and myofilament overlap. A reaction-diffusion model of the half-sarcomere further suggests that diffusional anisotropy may lead to modest adenine nucleotide gradients in the myoplasm under physiological conditions.

INTRODUCTION

Spatiotemporal diffusion of adenine nucleotides regulates cardiac energetics and excitation-contraction coupling, by transporting ATP as a substrate for myosin ATPase, ion channels, and transporters (ATP-sensitive K^+ channel, Na^+/K^+ pump, and sarcolemmal and sarcoplasmic reticulum Ca^{2+} ATPases) and the phosphocreatine shuttling pathway (1,2). Under physiological and pathological conditions, the irregular subcellular ultrastructure may lead to the development of nucleotide gradients that could affect nucleotide-dependent processes (3,4). Experimental and theoretical studies suggest that diffusion of ATP, its metabolites, and other small molecules is hindered within muscle cells (5–8). Recent studies have also implicated subcellular structures including mitochondria, transverse tubules, and the sarcoplasmic reticulum among the barriers contributing to hindered ionic and nucleotide diffusion within myocytes (5,9).

Within the myofibril, the thick and thin filaments form a dense hexagonal lattice (with <20-nm interfilament spacing) that, independent of organelle-scale features, has been suggested to influence the rate of nucleotide diffusion (7), and hence the development of concentration gradients, within a substantial fraction of the cell volume (4). The hexagonal lattice of the myofibril is aligned with the radial axis of the cell, and evidence suggests (9,10) that nucleotide diffusion along radial axis is slower than the longitudinal axis, along which the largely linear filaments are aligned. In particular, Shorten and Sneyd (9) have predicted, using cryo-electromagnetic (cryo-EM) resolution models of the thin and thick filaments, that the skeletal myofibril lattice imparts diffusional anisotropy, in line with spectroscopic evidence (6,7,11). Given that ATP consumption is highly regulated in cardiac cells and dysregulated under pathological conditions (12,13), we sought to quantify the magnitude of diffusional anisotropy in cardiac cells and its impact on nucleotide dynamics during pulsatile ATPase activity.

The extrapolation of Shorten and Sneyd's findings in skeletal muscle cells to heart cells likely depends on specific structural properties of the cardiac myofilaments and sarcomere. For example, wider myosin and actin filament distances, d_{ma}, are reported for cardiac myocytes compared with skeletal muscle (18.3 nm (14) vs. 16.5 nm (15)). Furthermore, because diffusion is inherently a macroscopic phenomenon dependent on molecular-scale attributes such as the molecular structure, solvent-accessible surface area, and conformation, there may be a benefit in using atomic-resolution structural data. For instance, even at cryo-EM resolution, the inclusion of approximate geometries of the myosin heads in the myofibril was shown by Shorten and Sneyd (9) to significantly reduce the rate of diffusion in the myofibril. Hence, by utilizing recently available atomistic structural data (16–18) and myofibril lattice spacings appropriate for cardiac cells, refined estimates for nucleotide diffusion in the cardiomyocyte may be possible.

Our recent successes in describing small molecule diffusion in atomistic systems (19,20), and the availability of

Submitted February 26, 2013, and accepted for publication September 18, 2013.

*Correspondence: pkekeneshuskey@ucsd.edu

Editor: Daniel Beard.

0006-3495/13/11/2130/11 $2.00

http://dx.doi.org/10.1016/j.bpj.2013.09.020

reconstructions of the thin filament from x-ray crystallographic structures (17), enable the investigation of molecular structure on cellular scale diffusion, such as for nucleotides. Recent studies on Ca^{2+} diffusion in cardiac myocytes (21,22) and diffusion within the actin/myosin myofilament lattice (9) have used homogenization theory in describing diffusion of small molecules such as Ca^{2+} and ATP. This technique provides a simultaneous description of molecular and cellular length-scales, specifically by spreading out, or homogenizing the contribution of a periodic microscopic domain comprising a macroscopic domain (23–25). Hence, we extend our approaches with homogenization theory (26–28), to integrate microscopic myofibril geometries of arbitrary resolution into macroscopic, sarcomere-scale models of diffusion.

In this study:

1. We estimate the diffusional anisotropy of nucleotides in the cardiac myofibril using atomic resolution reconstructions of sarcomeric proteins, and
2. We investigate the effects of diffusional anisotropy on ADP gradients under physiological conditions.

We applied the homogenization approach proposed for skeletal myofibrils in Shorten and Sneyd (9), to the cardiac myofibril, utilizing newly available atomic-resolution models of the thin filament. Using a molecular-scale homogenization approach, we examined the extent to which variations in the diffusion constant due to filament overlap, cross-bridges density, and lattice spacing influence the transport of ATP and its reaction partners. We furthermore investigated the propensity for the formation of ADP gradients within a finite-element model of the half-sarcomere, in which ATP hydrolysis by the myosin ATPase and ADP/ATP exchange with the mitochondrion are included. We find that anisotropic adenine nucleotide diffusion, originating from the configuration of atomistic-resolution myofibril proteins, may promote radial concentration gradients within the cardiac sarcomere.

METHODS

Geometries

Two-dimensional (primitive) and three-dimensional (atomistic) lattices were created. The software GMSH, Ver. 2.7 (30), was used to create the primitive lattice unit cell based on Fig. 1 of Tanner et al. (31) (see Fig. S1 *a* in the Supporting Material) and includes two intact actin filaments at its center, four myosin thick filaments, and four actin thin filament halves at the cell boundary; cell boundaries are coaligned with the macroscopic axes, $\hat{e}$.

The filaments are invariant along the z axis, thus the effective diffusivity may be completely described using a two-dimensional formulation of Michailova et al. (2). Three reference models of the atomistic myofibril unit cell were created:

1. Both thin and thick filaments;
2. Only thin filaments; and
3. Only thick filaments.

All filaments were aligned along z. The reference distance between the thick (M) and thin (A) filaments, d_{ma}, is 18.3 nm, which was varied to investigate lattice spacing effects. An atomic-resolution reconstruction (PDB:2W4U) (32) and the myosin heads from the myosin-bound thin filament model (PDB:4A7F) (33) were used for the thin filament (TF) geometry (Fig. 1). Up to three bound myosin head pairs (at 120° angles) were fitted to the TF based on the PDB:4A7F structure (33). The thick filament was represented by a cylinder of radius 6 Å, because molecular reconstructions were unavailable at the time. We refer the reader to Liao et al. (34) and the Supporting Material for mesh generation details.

Homogenization

We numerically solve the homogenized diffusion partial differential equation for χ_k in Equation 7 and compute the effective diffusivity D_{ij} from Equation 8 using the finite-element solver FENICS (35). The solver assumes surfaces at the mesh outer boundary belong to the unit cell ($\Gamma\backslash\Gamma_\epsilon$); all other boundaries are impermeable and thus belong to Γ_e. We solved the weak form of the homogenization equation using a piecewise linear Galerkin finite-element method with the default direct linear solver. The solution is then applied to Equation 8 to yield the ith components of D (D_{ii}). We report the effective diffusion constant by its normalized value, $D \equiv D/D^{\epsilon}$. The protocol is validated in the Supporting Material. The code will be released at https://bitbucket.org/huskeypm/homogenization.

Reaction-diffusion model

To examine the impact of altered nucleotide diffusion within the sarcomere, we created a finite-element reaction diffusion model (4–9),

$$\frac{\partial ATP}{\partial t} = -\nabla \cdot D_{\mathrm{ATP}} \nabla ATP - J_{\mathrm{hydrolysis}} - J_{CK}, \qquad (1)$$

$$\frac{\partial ADP}{\partial t} = -\nabla \cdot D_{\mathrm{ADP}} \nabla ADP + J_{\mathrm{hydrolysis}} + J_{CK}, \qquad (2)$$

where ATP and ADP are MgATP and free ADP, respectively, $J_{\mathrm{hydrolysis}}$ is the rate of ATP hydrolysis,

$$ATP \rightarrow ADP + P_i. \qquad (3)$$

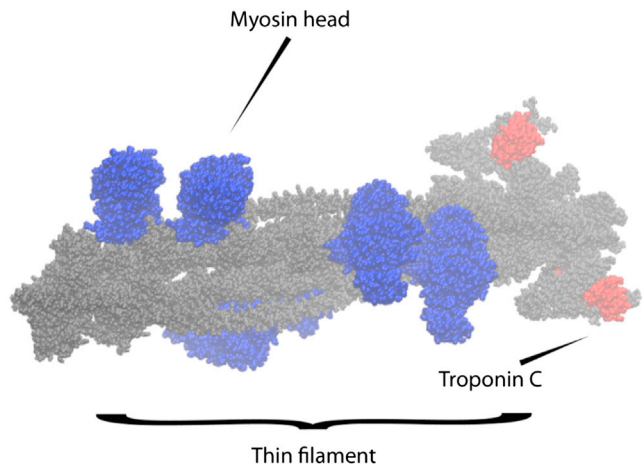

FIGURE 1 Atomistic thin filament model. Side view of thin filament (*gray*) with six bound myosin heads (three cross-bridges, *blue*). Troponin C is marked (*red*) for reference.

and J_{CK} is the rate of cytosolic creatine kinase reaction,

$$ATP + Cr \leftrightarrow ADP + PCr. \tag{4}$$

P_i, Cr, and PCr are inorganic phosphate, creatine, and phosphocreatine. We assumed that ATPase heads interacted with thin filament but activity was continuously distributed and restricted to the overlap region of the A-band (see Fig. 1 B of Vendelin et al. (36)); similarly, creatine-kinase (CK) activity was concentrated along the boundaries normal to the mitochondrion intermembrane space, and decreased linearly toward the center of the myofibril. At the interface between the cytosol and intermembrane space, we applied the boundary conditions

$$D_N \nabla N = J_{N,\text{diff}} \text{ for } N = ATP, ADP, \tag{5}$$

which control the rate of ADP entry into the mitochondrion and flow of synthesized ATP into the cytosol. The concentration of substrates P_i, Cr, PCr, as well as ATP/ADP in the intermembrane space, were treated as whole-cell values by our implementation of the ordinary differential equation model of van Beek (37). D_{ATP} and D_{ADP} in Selivanov et al. (4) represent the diffusion coefficients for ATP and ADP; we consider both an isotropic diffusion constant ($D_{ii} = D^\epsilon \cdot 1.0$, where $D^\epsilon = 145$ [μm^2/s]) and an anisotropic diffusion constant for the diffusing species determined from our homogenization models.

We modeled myosin ATPase activity, creatine kinase activity, and nucleotide exchange between the sarcomere and mitochondrion, using a myocardial metabolism model from van Beek (37). The van Beek model included mitochondrial synthesis of ATP from ADP via oxidative phosphorylation, hydrolysis of ATP ($J_{hydrolysis}$) in the myofibril, and diffusion of nucleotides between the intermembrane space (intermembrane space) and the myofibril (J_{diff}) as well as fluxes due to the creatine-kinase (CK) pathway (J_{CK}). The contribution of the adenosine nucleotide transporter (ANT) was implicitly represented by the intermembrane space diffusional fluxes, because reduced models and full models of mitochondrial coupling (e.g., via explicit models of ANT (36)) have been shown to yield similar results (37). Further details of the model geometry, integration of the ordinary and partial differential equation models, and their solution are in the Supporting Material.

THEORY

We present a brief mathematical formulation of the homogenized diffusion equations; a lengthier treatment of this approach can be found in the literature (21,22,24). Given a macroscale geometry $\Omega_m \subset \mathbb{R}^3$, the time-dependent diffusion problem is to find an ionic concentration function $c{:}\Omega_m \times [0,T] \rightarrow \mathbb{R}$ such that

$$\frac{\partial c}{\partial t} = \nabla \cdot D\ \nabla c \quad \text{on } \Omega_m, \tag{6}$$

where D is an unknown effective diffusion tensor. A function f representing the net effect of any ionic sinks or sources is given for the initial condition $c(x,0) = f(x,0)$ for all $x \in \Omega_m$ and the boundary conditions $c(x,t) = f(x,t)$ for $x \in \partial\Omega_m$, $t \in [0,T]$. The forcing term f represents the net effect of any ionic sinks or sources on $\partial\Omega$.

We assume that Ω_m has two length scales of interest, $\mathbf{x}$ and $\mathbf{y} := \mathbf{x}/\epsilon$. Here, ϵ is small compared to the dimensions of Ω and it is assumed that Ω is periodic at the $\mathbf{y}$ scale; a unit cell in this lattice is denoted Ω, and the accessible region therein as Ω_ϵ. We further assume that D is a function of the $\mathbf{y}$ scale only, i.e., that $D(\mathbf{x},\mathbf{y})$ can be written as $D^\epsilon(\mathbf{y})$ (in the application context here, this assumption on D implies that a Ca^{2+} ion's diffusion is governed by its location relative to nearby myosin and actin molecules, but not its location in the larger lattice of thick and thin filaments). The homogenization is carried out by expanding c in terms of powers of ϵ (i.e., $c = \sum_i c_i \epsilon^i$) and writing ∇ as a scaled gradient operator (i.e., $\nabla = \partial_x + \epsilon^{-1}\partial_y$). This results in the $\mathbf{y}$-scale steady-state problem: find $\chi{:}\Omega\epsilon \rightarrow \mathbb{R}$ such that

$$\begin{aligned}
&\nabla \cdot \left(D^\epsilon_{ij} \left(\delta_{jk} + \frac{\partial \chi_k}{\partial y_j} \right) \right) = 0, && \text{on } \Omega_\epsilon, \\
&\left(D^\epsilon_{ij} \left(\delta_{jk} + \frac{\partial \chi_k}{\partial y_j} \right) \right) \cdot \hat{n} = 0, && \text{on } \Gamma_\epsilon := \partial\Omega_\epsilon, \\
&\left(D^\epsilon_{ij} \left(\frac{\partial \chi_k}{\partial y_j} \right) \right) \cdot \hat{n} = 0, && \text{on } \Gamma \setminus \Gamma_\epsilon := \partial\Omega \setminus \partial\Omega_\epsilon,
\end{aligned} \tag{7}$$

where Γ_ϵ corresponds to a molecular boundary and $\partial\Omega\backslash\partial\Omega_\epsilon$ refers to all other boundaries, the diffusion coefficients D^ϵ are experimental inputs, and periodicity of χ with respect to opposite sides of Γ_ϵ is enforced. Given solutions for χ, the coefficients of the effective diffusion tensor can be computed via

$$D_{ij} = \frac{1}{|\Omega|} \int_{\Omega_\epsilon} D^\epsilon_{ij}(y) \left(\delta_{jk} - \frac{\partial \chi_k}{\partial y_j} dy \right), \tag{8}$$

where Ω is the unit cell volume.

RESULTS

Validation of homogenization model

As a preliminary step, we show that our implementation of the homogenization protocol applied to a layered n-dimensional system and a lattice of cylinders of varying diameters is in strong agreement with analytical predictions (see the Supporting Material). We then compared our homogenization implementation against results predicted by Shorten and Sneyd (9). In their study, a unit cell containing two myosin filament quarters and two actin filament halves arranged with a myosin/actin spacing, d_{ma} of 16.5 nm (typical of skeletal muscle (15)), was used for the solution of the homogenization equation (see Fig. S1 *b*). We used a larger unit cell (the primitive mesh) to facilitate integrating intact molecular models in the next section. We solved Eq. 7 on the primitive mesh and report the homogenized field along x, χ_x, for particles of diameter 0 and 6 nm in Fig. S2. The χ_i field indicates the relative impact of diffusional barriers on the effective transport along the ith direction. Generally speaking, $\chi_x \approx 0$ signifies regions where diffusion essentially unhindered, whereas deviations from zero signify strong diffusional hindrance. Based on Eq. 8, if the gradient

$\partial\chi_x/\partial y_x$ is zero (as one expects for $\chi_x = 0$), the effective diffusion constant, D_{ij}, is equal to its reference value, $D^{\epsilon}{}_{ij}$. When $\chi_x! = 0$ in the neighborhood of diffusional obstacles, nonzero values for $\partial\chi_x/\partial y_x$ will in general reduce the integrand of Eq. 8 and yield a smaller effective diffusion constant relative to its reference value.

We observed that positive gradients predominated over negative gradients arising from the filament diffusional barriers, which reduced the integrand in Eq. 8 and hence, D_{ij}. The predominance of nonzero gradients for the 6-nm substrate modeled relative to a 0-nm substrate suggests that the former has a smaller effective diffusion constant. The magnitude and profile of χ_x predicted by our implementation for the large unit cell qualitatively agree with solutions shown in Fig. 5 of Shorten and Sneyd (9) (not shown).

Fig. 2 compares our predictions for the x component (orthogonal to filament axis) of the effective diffusion constant, D_{xx}, at d_{ma} =16.5 nm using Eq. 8 with estimates from the literature (Fig. 6 of Shorten and Sneyd (9)). In qualitative agreement with Shorten and Sneyd, we observe that D_{xx} decreases linearly with increasing particle sizes until converging to zero as the particle diameter (8 nm) approaches the mean free distance between filaments. For substrates smaller than 1 nm, such as the nucleotides at the focus of our study, $D_{xx} \approx 68\%$ of its bulk value. We also compared our predictions against the Hashin-Shtrikman (HS) bound from Auriault et al. (26) ($D = \phi/(2 - \phi)$), where ϕ is the accessible volume fraction), and found exceptional agreement for all but the smallest volume fractions (near 8-nm particle diameters). The deviation is likely due to the nonuniform filament radii. For a d_{ma} value typical of cardiac tissue

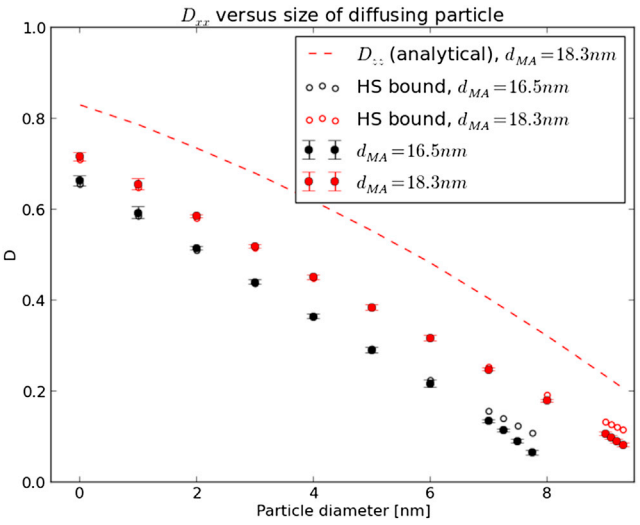

FIGURE 2 Effect of myofibril lattice spacing on D. Predictions of the effective diffusion constant for myosin/actin spacings of 16.5 and 18.3 nm along the transverse direction based on the primitive unit cell in Fig. S1 *a* in the Supporting Material as a function of diffusing particle size. Error bars represent the 95% confidence interval based on three trials of differing mesh resolutions. We include an analytical estimate for D parallel to the filaments (Dzz) for comparison. To see this figure in color, go online.

(18.3 nm) (14), we report a lesser extent of hindrance along the x direction, which is still less than hindrance along the z axis. $D_{xx} \approx 0.72$, $D_{zz} \approx 0.82$, for substrate diameters <1 nm.

Diffusivity on large unit cell with atomistic-representation of thin filaments

We incorporated an atomistic representation of the thin filament into the unit cell geometry to determine its impact on diffusion. Solutions for χ_x and χ_z are shown in Fig. 3. The value χ_x for the atomistic mesh resemble those for the primitive mesh, with positive gradients predicted to the left of molecular boundaries, and negative on the right. Notable differences, however, are reported for the thin filament, as the protruding Troponin complex and bound myosin heads perturb χ_x and χ_z. Inclusion of the molecular geometries reduce D_{xx} and D_{zz}, in a similar fashion to the estimates of Shorten and Sneyd (9) when cryo-EM resolution myosin heads were included. Our predictions indicate $D_{xx} = 0.42$ (Table 1) and $D_{zz} = 0.59$, versus 0.72 and 0.82 predicted for the primitive mesh (Fig. 2); our estimate are within 5% of the HS bound. The 95% confidence interval in D_{ii} based on varying the mesh resolution was <0.03 (see the Supporting Material), thus we believe differences in reported the D_{xx} values are significant.

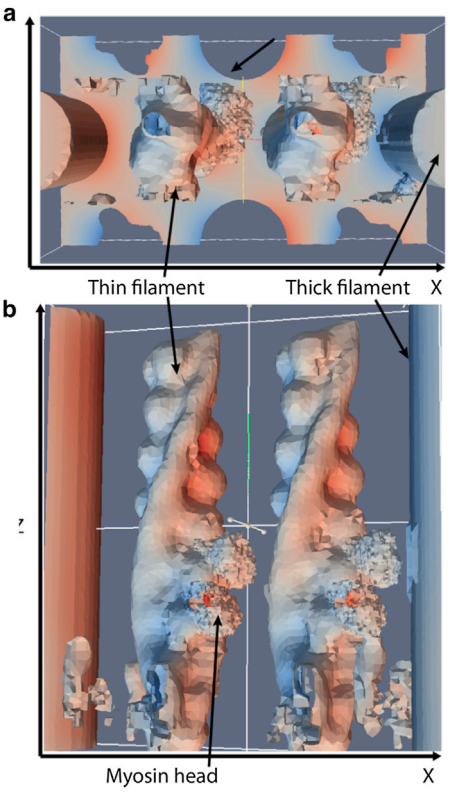

FIGURE 3 Solutions of the homogenized fields for a unit cell with atomistic-resolution geometries: (*a*) χ_x; (*b*) χ_z. Thin filament geometries of outer boundary are hidden for clarity.

TABLE 1 Predicted effective diffusion constants with respect to myosin/actin overlap

Region	$[D_{xx}, D_{yy}, D_{zz}]$	ϕ	HS[a] bound (D_{xx})
A-band (filament overlap)	[0.42, 0.45, 0.59]	0.61	0.44
I-band (thin filament only)	[0.59, 0.64, 0.75]	0.77	0.62
H-zone (thick filament only)	[0.70, 0.71, 0.82]	0.82	0.69

[a]HS is Hashin-Shtrikman bound for transverse diffusion rate based on volume fraction, ϕ.

Influence of lattice geometry on ATP diffusional anisotropy

We hypothesized that increased thin and thick filament overlap influences diffusional anisotropy. Table 1 provides D_{ii} for the I-band (thin filament-only), the filament overlap region of the A-band, and H-zone (thick filament only). The overlap region presented the largest hindered diffusion (D_{ii} = [0.42, 0.45, 0.59]), the I-band less so (D_{ii} = [0.59, 0.64, 0.75]), and the H-zone with the least (D_{ii} = [0.70, 0.71, 0.82]). The magnitude of D was correlated with the accessible volume fraction and HS bound. We further hypothesized that altered interfilament spacing within the overlap region would modulate D; indeed, in Table 2 we demonstrate for a myosin-bound filament that a 10% decrease in d_{ma} leads to a reduction in D_{xx} (0.26 vs. 0.34) versus an increase in D_{xx} (0.34 vs. 0.44) for a commensurate increase in d_{ma}.

We sought to understand the influence of thin filament-bound myosin heads on diffusivity. We estimated D_{ii} for zero to three cross-bridges formed between myosin heads and each thin filament. Our results in Table 3 indicate that D_{ii} decreases with increasing cross-bridge density based on d_{ma} = 18.3 μm. Although the differences in D between sequential additions of myosin heads are comparable to our estimates of standard error (see the Supporting Material), there is a 20% difference between the zero- and three cross-bridge states, which we deem significant.

Anisotropic diffusion in a sarcomere reaction-diffusion model

We speculated that hindered, anisotropic diffusion would enhance ADP gradients in the myofibril lattice relative to the unhindered, isotropic constant. We thus simulated nucleotide diffusion within a half-sarcomere model for the isotropic bulk and anisotropic diffusion constants, D^{ϵ} and D, where D is based on the three cross-bridge lattice, d_{ma} = 16.4 nm model, as well as with (+CK) and without (−CK) creatine kinase activity. Resting levels of ATP and ADP (+CK, [ATP] ≈ 5.92 mM, [ADP] ≈ 0.055 mM) were sustained for each 300-ms beat interval through 6 s of simulation (independent of the diffusion constant) and evidence the stability of the model (see Fig. S8 *a*); moreover, while the concentration of ATP changes <3%, peak [ADP] is twofold larger than resting levels (≈0.11 mM) and consistent with predictions from Van Beek (see Fig. 10 in van Beek (37)). In Fig. 4 *a* we report a 300-ms beat interval, over which [ADP] follows the time course of $J_{\text{hydrolysis}}$ (see Fig. S9) with a maximum at 5.27 s; [ADP] is marginally higher in the overlap region relative to the I-band and near the intermembrane space, with the largest variations observed for the anisotropic diffusion constant (*red*) versus isotropic (*black*). We report the two-dimensional ADP distribution at peak J_{ATP} in Fig. S10, which suggests a [ADP] gradient develops along the radial (y) direction, stemming from the higher concentration of ADP in the myofibril relative to the intermembrane space. The radial ADP gradient summarized in Fig. 5 was approximately twofold higher for D relative to D^{ϵ} (∇ [ATP] ≈ 10 μM/μm for isotropic relative to ~20 μM/μm for anisotropic).

It was reported in van Beek (37) that CK buffers ADP fluctuations arising from pulsatile ATPase activity, thus we compared the scale of ADP gradients in absence of CK (−CK) and their dependence on the anisotropic diffusion constant. We reduced the CK rate constants by 98%, which decreased the resting [ADP] (to 0.01 mM from almost 0.06), and nearly doubled the peak [ADP] (to 0.14 mM from 0.11). Without the consumption of ADP by the myofibril CK pathway, elevated ADP pools persisted in the cytosol and increased the time required to restore resting levels of the nucleotide (0.20 s relative to 0.08 s for CK present). Radial ADP gradients were negligibly increased for the isotropic CK-absent case relative to CK-present, whereas the gradients for the anisotropic case increased by <30% (see Fig. S10 and Fig. 5).

It has been speculated that nucleotide diffusion rates within the myofibril may deviate significantly from measurements in bulk water (36). Indirect estimates have ranged considerably, with a recent study suggesting reductions as

TABLE 2 Predicted effective diffusion constants with respect to myosin/actin lattice spacing, d_{ma}, for the thin filament with bound myosin heads

d_{ma}, nm	$[D_{xx}, D_{yy}, D_{zz}]$	ϕ	HS[a] bound (D_{xx})
16.43	[0.26, 0.26, 0.37]	0.45	0.29
18.26	[0.34, 0.35, 0.46]	0.53	0.36
20.08	[0.44, 0.44, 0.57]	0.61	0.44

[a]HS is Hashin-Shtrikman bound for transverse diffusion rate based on volume fraction, ϕ.

TABLE 3 Predicted effective diffusion constants for actin with varying number of bound myosin heads

d_{ma}, nm	Cross-bridges	$[D_{xx}, D_{yy}, D_{zz}]$	ϕ	HS[a] bound (D_{xx})
18.26	0	[0.42, 0.45, 0.59]	0.61	0.44
18.26	1	[0.38, 0.41, 0.54]	0.58	0.41
18.26	2	[0.38, 0.37, 0.50]	0.56	0.39
18.26	3	[0.34, 0.35, 0.46]	0.53	0.36

[a]HS is Hashin-Shtrikman bound for transverse diffusion rate based on volume fraction, ϕ.

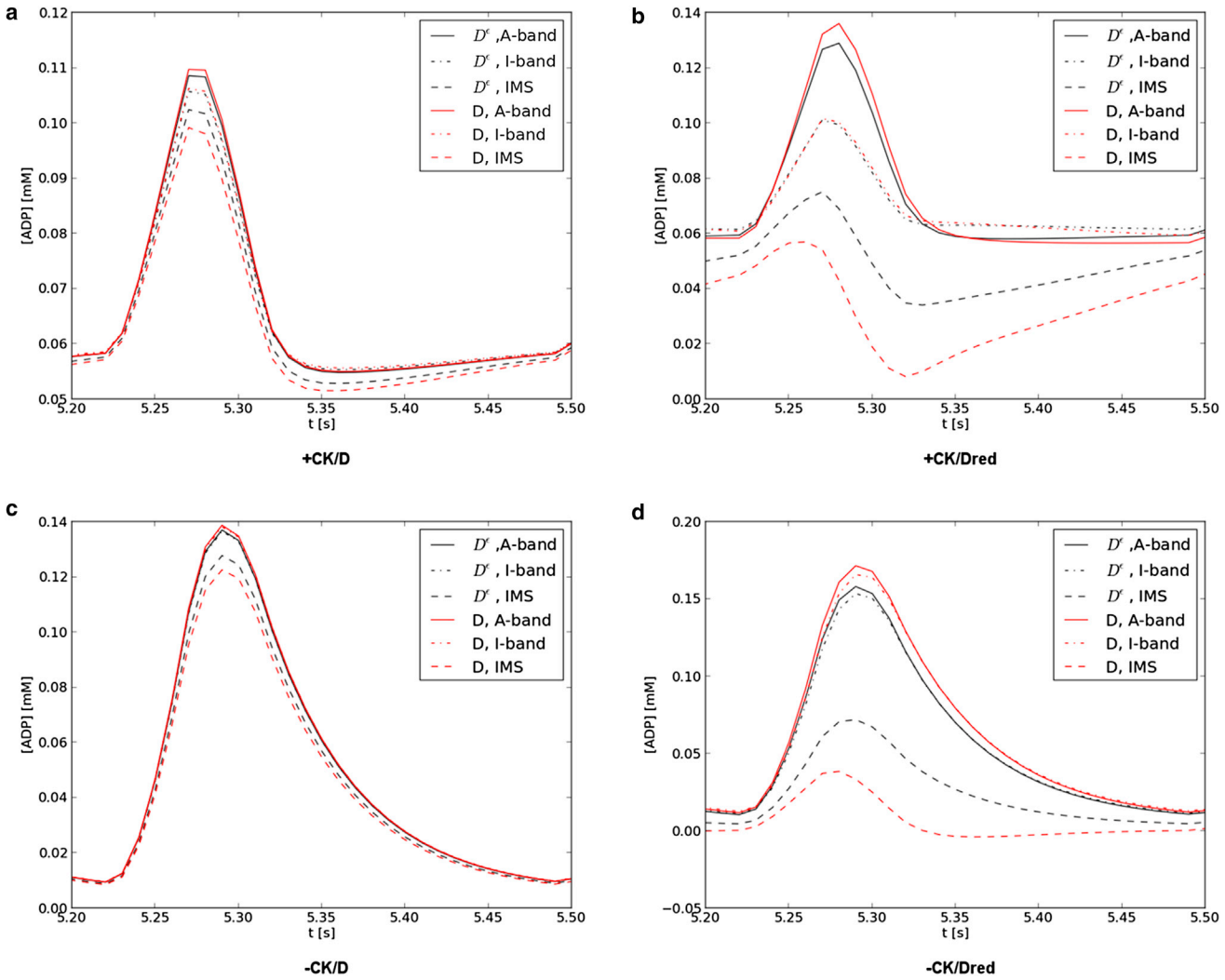

FIGURE 4 ADP concentration profiles. [ADP]at several sarcomere locations with CK (*a* and *b*) and without (*c* and *d*), and with a normal (*a* and *c*) or 10-fold reduced (*b* and *d*) diffusion constant are given. [ADP] is reported at the filament overlap region of the A-band (*solid*), I-band (*dashed*), and adjacent to the intermembrane space (*dot dash*) for the isotropic (*black*) and anisotropic (*red*) diffusion constants. ADP profiles are in agreement with Fig. 10 of Van Beek (37). To see this figure in color, go online.

low as one-thousandth of the bulk rate are necessary for consistency with observations of ATP compartmentalization in the myofibril (4). We reduced the diffusion constant by 90% to examine its impact on ADP distribution. We observed a substantial increase in peak [ADP] within the myofibril ($\approx$20%) and reduction in ADP at the intermembrane space ($\approx$30–40%). When CK was active, [ADP] was reduced by 30% within the I-band (where CK activity is assumed to be maximal) and the intermembrane space [ADP] appeared to overshoot the resting concentration. This overshot may be a limitation of the model, as we applied fluxes based on the average concentration of the nucleotides in the sarcomere (J_{average}), not their local concentrations (J_{local}), which would locally deplete ADP when $J_{\text{average}} > J_{\text{local}}$. Nevertheless, we observe clear distinctions between the anisotropic and isotropic diffusion constants that arise when the constant was reduced significantly, as shown in Fig. 5 (and see Fig. S11).

DISCUSSION

Atomistic-scale features induce diffusional anisotropy in myofibril lattice

Prior studies successfully applied homogenization to estimate diffusional anisotropy in cellular and subcellular environments (9,21,22). Homogenization requires the macroscopic (cellular) and microscopic (subcellular or molecular) spatial scales to be decoupled, as quantified by the $y = x/\epsilon$ limit (see Theory). This condition is satisfied for the myofibrils, because the unit cell (~50 nm per side) is an order-of-magnitude smaller than the μm-scale dimensions of the sarcomere. Hence, the success of Shorten and Sneyd (9) in providing compelling evidence that the myofibril lattice contributes significant diffusion hindrance and anisotropy. Our studies extend their work by adding atomistic-resolution detail for the thin filament and indicate

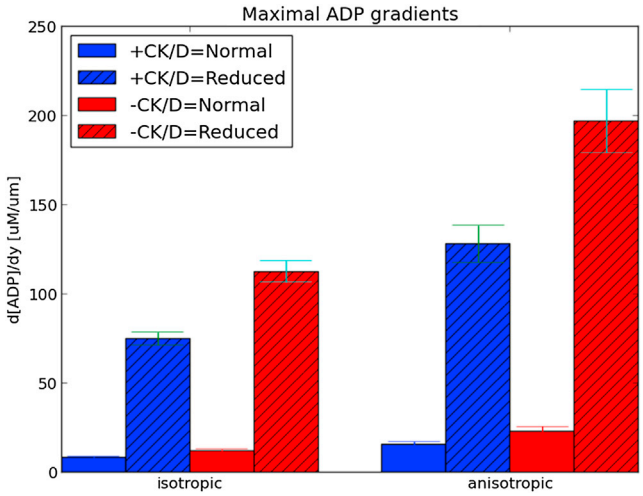

FIGURE 5 Maximal ADP gradients. Comparison of ADP gradients at $t \approx 5.3$ s in the presence (*blue*) and absence (*red*) of CK activity, and with normal (*solid*) and 10-fold reduced (*patterned*) diffusion coefficients. Gradients are defined based on [ADP] at the A-band relative to the interface with the intermembrane space. Error bars represent 95% confidence interval based on 10 trials where the diffusion constant was randomly varied within one standard deviation (0.035) of the estimated values from homogenization (see the Supporting Material). To see this figure in color, go online.

greater diffusional hindrance than estimated by lower resolution geometries. Moreover, our technique provides what we believe is a novel bridge between atomistic-resolution reconstructions of macromolecules and cellular-scale signaling processes.

The ratio of our D_{xx} to D_{zz} estimates in the filament overlap region were ~70% $\pm$ 0.027 under a variety of lattice spacings and cross-bridge densities, which agrees with recent image correlation spectroscopy estimates (0.69–0.70, Table 1 (11)) and observations of other small molecules (0.72–0.74) (6,7). In fact, our predictions using three cross-bridges per filament at 18.3 μm ($D_{xx} = 0.34$ and $D_{zz} = 0.46$) are strikingly close to the recent image correlation spectroscopy estimates, which revealed radial and longitudinal diffusion constants that are 28 and 45% of the 183 [$\mu m^2/s$] isotropic rate measured in water. In contrast, our primitive unit cell predicts a D_{xx}/D_{zz} ratio of ~82%, which clearly overestimates transverse diffusion rates. This finding demonstrates that atomistic-resolution, macromolecular models of the filaments yield superior predictive power for modeling diffusion in complex environments.

Interestingly, our estimate of diffusional anisotropy along x ($D_{xx} = 0.26$) at $d_{ma} = 16.43$ nm, which approximates the distance used by Shorten and Sneyd (9), is significantly smaller than predicted by their approach ($D_{xx} = 0.72$). We suspect that the accessible volume fraction in our model is significant smaller than the model of Shorten and Sneyd, which would lead to a different scale for the effective diffusion constant. One explanation for the difference is that our molecular resolution geometries occupy a greater volume than the cryo-EM structures used in their study. Hence, accurate determination of the diffusivity is contingent upon a reasonable assessment of the molecular volume, for which we believe atomistic-resolution data are ideally suited. At a larger d_{ma} typical of cardiac tissue (18.3 nm), D_{xx} is 30% of the bulk value, the less restrictive packing may permit the diffusion of larger substrates than accommodated by the skeletal muscle myofibril; it is possible that the more rapid diffusion rates help maintain myofilament energetics in a reaction-limited regime (3), especially given the high oxidative demands of cardiomyocytes.

Nucleotide diffusion is dependent on myofibril configuration

During contraction, the myofibril lattice spacing decreases and concomitantly drives the myosin heads toward the actin subunits on the thin filament (14); given appropriate substrates, cross-bridges may be formed and drive contraction. Three regions of the sarcomere—the I-band, the filament overlap region of the A-band, and the H-zone—differ with respect to the presence or absence of thin and thick filaments. We anticipated that each region would have a sufficiently different volume fraction depending on the filaments present, and this in turn would influence D. Our results confirm this hypothesis, as we observed decreases of 30–40% between the filament overlap region and the I-band or H-zone. We hypothesize that nucleotide diffusion depends on the longitudinal position along the myofilament, yet a firm conclusion awaits a more complete model of the I- and H-zones, including structurally important structural proteins such as titin, obscurin, and nebulin (38).

In the overlap region of the A-band, the myosin-actin filament spacing varies as a function of sarcomere length; this property provides a structural basis for the Frank-Starling law, whereby increased sarcomere length is associated with enhanced force generation (39). Because the cell is stretched during diastole, transverse constriction will reduce the effective volume fraction, while systolic shortening of the sarcomere and expansion of the myofilament lattice would have the opposite effect; hence, we hypothesized that these structural changes would hinder diffusion to greater and lesser degrees, respectively, relative to the resting configuration. Indeed, our results demonstrate a positive correlation between effective diffusivity and myofilament spacing, with smaller myosin-actin distances demonstrating a greater extent of hindered diffusion and anisotropy. Thus, regardless of other proteins that may exist between the filaments, nucleotide diffusion may be modestly sensitive to changes in lattice spacing; this sensitivity may be more apparent for conditions in which myofibril strain and sarcomere length are increased by elevated diastolic pressures, such as dilated cardiomyopathy and heart failure (40).

The sliding of filaments is driven in part by the association of myosin heads to actin subunits comprising the thin

filament. In Shorten and Sneyd (9), the presence of myosin heads in the skeletal myofibril was found to reduce D_{xx} by ~15% relative to the filament-only geometry. In agreement with their findings, we observe a 20% decrease in D_{xx} between the three-crossbridge-per-TF case relative to the crossbridge-free case (0.34 vs. 0.42); our prediction is also consistent with estimates from analytical bounds (26,41) using the corresponding accessible volumes ($D_{xx} = 0.36$ vs. $D_{xx} = 0.43$). In fact, we find that a linear-least-squares fit of D_{xx} from the HS bound to our estimated D_{xx} (and D_{yy}) across all overlapping geometries is in quantitative agreement with an $R^2 = 0.97$ (not shown). That is, the diffusivity is determined almost exclusively by the accessible volume fraction. Hence, our predictions are unlikely to change significantly if the myosin heads were solely tethered to the thick filament and not bound to the thin filament, as would be expected during relaxation of the myofibril. In theory we could predict D_{xx} based on the volume of proteins in the myofibril using the HS bound, including those not directly associated with the filaments, regardless of their location or binding configuration. However, we observed that the bound underestimated the extent of hindered diffusion for large particles corresponding to volume fractions below roughly 20% (Fig. 2). Given that the volume fraction of a cell may fall within this range (0.19–0.27) (42), it is likely the HS bound would underestimate the extent of diffusional hindrance for even small particles. This shortcoming provides strong justification for advanced models of diffusion in crowded environments, such as Brownian dynamics (42,43), Monte Carlo simulations (9,10), and homogenization (9).

Nucleotide diffusional anisotropy impacts the spatial-temporal distribution of ADP in sarcomere

As the byproduct of ATPase activity during contraction, ADP is an important substrate for the reestablishment of resting ATP concentrations, directly through oxidative phosphorylation within the mitochondrion and indirectly through the creatine kinase pathway. The interplay among the distribution and activity of metabolic enzymes, the localization of substrates, and substrate diffusion rates between enzymatically active regions, are important constraints for energy delivery within the cell (8). Early numerical studies of mitochondrial respiration in a two-dimensional representation of the sarcomere suggested the development of slight cytosolic ADP gradients ($\approx 20\ \mu M/\mu m$) (36). These gradients were significantly amplified when a 10-fold reduced diffusion constant was used, based on estimates from confocal imaging of redox (44) and mitochondrial membrane potentials under substrate-deprived conditions (45). More recently, by fitting a reaction-diffusion model to experimental measurements of myosin ATPase activity (4), it was suggested that the diffusion constant may be up to three orders-of-magnitude smaller than its bulk value, which was then shown to promote significant radial ADP gradients in the sarcomere. While there are apparent discrepancies between these indirect measurements of the nucleotide diffusion constant and direct spectroscopic measurements, our homogenization method provides a framework for quantifying the molecular-scale contributions to hindered diffusion and anisotropy for a given reference diffusion constant, and describing their impact on diffusion gradients within the sarcomere.

Our simplified sarcomere model demonstrates localization of ADP and the development of ADP gradients under physiological conditions, similar to findings from prior studies (4,36). To estimate the magnitude of ADP gradients, we performed reaction diffusion simulations comparable to those performed by Vendelin et al. (36), using the directly-measured bulk rate (145 $\mu m^2/s$) and a 10-fold reduced rate (1.45 $\mu m^2/s$) motivated by indirect measurements (4,36,44,45). Our findings confirm that radial ADP gradients develop during contraction (36), due to the localization of myosin ATPases within the myofibril bundle versus the mitochondrial intermembrane space (46), as well as along the longitudinal direction CK activity concentrated along the I-band and M-line (46); these longitudinal ADP gradients are all but abolished upon cessation of CK activity.

Our predictions of the effective diffusion tensor within the myofibril, which suggest substantially greater diffusional hindrance transverse to the myofilaments relative to parallel, nearly double the magnitude of radial ADP gradients in the sarcomere for all cases we considered. Upon reduction of creatine kinase activity, a pathway known for dampening ADP oscillations during contraction (8,37), we found that radial ADP gradients were increased upwards of 30%. A 10-fold reduction of the diffusion constant toward values inferred indirectly from measurements of ATPase activity lead to the largest enhancement of ADP gradients, which were maximized with the anisotropic diffusion constant. While direct methods suggest reduced diffusion coefficients within one order of magnitude of its value in dilute solution, it has been suggested that substantially slower constants inferred from myosin ATPase activity may reflect the average diffusional rate between the catalytic sites and cell periphery. Hence, the results here may characterize a range in potential ADP gradients encountered in the cytosol. Additionally, whereas the localization of ADP is dependent on our assumptions of protein distributions and sarcomere geometry based on Vendelin et al. (36), our predictions of metabolite distribution shed insight into important constraints for oxidative phosphorylation (4) and metabolism as a whole.

Despite these observations, there is considerable evidence to suggest that ATP hydrolysis is reaction-, not diffusion-limited (3). At the myofibril level, it is probably no accident that ATP hydrolysis and synthesis machinery are not diffusion-limited, because it relieves the constraint that the contractile fibers could impose on the diffusion of substrates.

Nevertheless, conditions that significantly alter diffusion distances, such as large myofibrils (47) and pathological remodeling (48), or significant deviations in oxygenation at high workload (3), could shift metabolism to a diffusion-limited regime. In which case, ADP gradients may develop within the myofibril; to understand their impact on metabolic signaling, accurate estimates of anisotropic diffusion constants from experiments (6,7,11) or theoretical constants such as ours may be of considerable importance.

Limitations

The relative compactness of the myofibril lattice gives rise to substantial anisotropy in the diffusion of small molecules, which is further modulated by changes in lattice spacing and cross-bridge configuration. Lattice changes were done independently of any molecular changes, such as known conformational changes of the troponin complex (49,50) during rigor, but we anticipate that their effects on diffusivity are likely secondary to changes in lattice spacing and overlap. Lastly, substitution of our simplistic model of the thick filament with a molecular-scale reconstruction could improve our estimates of its contribution to hindered diffusion (51).

The primary nonsteric factors that could additionally influence diffusional anisotropy include hydrodynamic effects and electrostatic interactions (42). Hydrodynamic interactions scale roughly with the relative size of the diffusing substrate to the separation between obstacles (52); based on our filament model, the nucleotide radii are one-tenth of the filament spacing and thus we believe hydrodynamic effects are modest. Larger diffusing molecules, such as CaM, and diffusion adjacent to walls, would lead to more appreciable effects (9). Electrostatics may also influence the nature of diffusion (19,20), especially given the net negative charges of the nucleotides. Based on our model, the distance between fibers is almost 20 nm, which is several fold greater than the Debye length (7 Å at physiological ionic strength) and thus electrostatic interactions are likely to be modest.

However, the cell cytosol is a crowded domain where interactions between diffusing substrates and crowders can significantly impact reaction-diffusion dynamics (42,53). Similarly, additional structures intertwining with the thin/thick filament lattice, such as myosin binding protein C, as well as other molecular players including kinases associated with phosphorylation of troponin and myosin and diffusing entities like calmodulin (1), could impact substrate diffusion. Explicit consideration of crowders would be expected to decrease the accessible volume and in turn, the effective diffusion rate. Concurrently, crowding results in reduced intermolecular separations that may approach the Debye length expected at physiological ionic strengths. Under such conditions, electrostatic and hydrodynamic interactions may be more significant factors, particularly for charged substrates like the nucleotides. Extension of the homogenization approach to include external fields and hydrodynamic considerations could address these limitations.

Our half-sarcomere model does not explicitly consider the spatial-temporal dynamics of the CK substrates Cr and PCr, nor P_i, of which at least PCr demonstrates anisotropic diffusion (54). We further assumed a spatially uniform diffusional flux of nucleotides across the intermembrane space, which may be inadequate if the distribution of adenosine nucleotide transporters responsible for nucleotide exchange between the mitochondrion and intermembrane space is heterogeneous. Related to this point is our use of a simplified mitochondrial model; more sophisticated models such as Cortassa et al. (55) and Beard (56), for which the mitochondrial potential and NADH-dependent reactions are considered, as well as the contribution of the adenylate kinase pathway, may improve the accuracy of our predictions.

Furthermore, we used a coarse description for the nonuniform distribution of ATPase and CK activity, which could be improved with more detailed data. Our simulation domain was represented by a simple geometry, although studies such as ours (20,57,58) and those of others (59,60) have demonstrated a significant influence of realistic geometries on small-molecule diffusion. These factors all have the potential to alter the location and magnitude of the substrate gradients developing during the course of a heartbeat, and warrant further refinement. Nevertheless, the integration of molecular-scale based predictions of diffusional anisotropy with a simplified model of nucleotide dynamics constitutes an important step toward a realistic depiction of metabolism within the sarcomere.

CONCLUSIONS AND FUTURE WORK

We have demonstrated the contribution of myofibril macrostructures to the apparent anisotropic diffusion of ATP and ADP. The anisotropy arises due to the diffusional restrictions imposed by the impermeable surfaces of molecular structures. Long-range forces, such as electrostatic interactions, and substantial conformational flexibility can be expected to further nuance the diffusional picture. We have demonstrated that the contribution of atomistic-resolution, macromolecular structural data to macroscopic diffusional processes can be readily integrated into conventional subcellular models of diffusion. Although the necessity of including atomistic-resolution details for accurate cellular modeling may seem to be a daunting task, the fact that homogenization of molecular scale features over a macroscopic region yields surprising accurate results suggests that simultaneous modeling molecular and cellular features in some cases could be pursued by homogenizing representative unit cells at several separable length-scales. As such, homogenization simulations can inform cellular simulations (58) and leverage macromolecular electrostatic descriptions (19) in regimes where molecular-scale physiochemical

properties profoundly influence diffusion-dependent aspects of molecular signaling.

SUPPORTING MATERIAL

One table, eleven figures and supporting information are available at http://www.biophysj.org/biophysj/supplemental/S0006-3495(13)01068-0.

P.M.K.-H. thanks Pranay Goel, Adarsh Krishnamurthy, and Sukriti Dewan for many helpful discussions.

This work was supported by the National Institutes of Health, the National Science Foundation, the Howard Hughes Medical Institute, the National Biomedical Computation Resource, and the National Science Foundation Supercomputer Centers. P.M.K.-H. was supported by American Heart Association award No. 13POST14510036.

REFERENCES

1. Bers, D. 2001. Excitation-Contraction Coupling and Cardiac Contractile Force, Vol. 1, 1st Ed. Kluwer Academic Publishers, Dordrecht, The Netherlands.
2. Michailova, A. A., J. J. Saucerman, …, A. D. A. McCulloch. 2005. Modeling regulation of cardiac KATP and L-type Ca^{2+} currents by ATP, ADP, and Mg^{2+}. *Biophys. J.* 88:2234–2249.
3. Kinsey, S. T., B. R. Locke, and R. M. Dillaman. 2011. Molecules in motion: influences of diffusion on metabolic structure and function in skeletal muscle. *J. Exp. Biol.* 214:263–274.
4. Selivanov, V. A., S. Krause, …, M. Cascante. 2007. Modeling of spatial metabolite distributions in the cardiac sarcomere. *Biophys. J.* 92:3492–3500.
5. Illaste, A., M. Laasmaa, …, M. Vendelin. 2012. Analysis of molecular movement reveals latticelike obstructions to diffusion in heart muscle cells. *Biophys. J.* 102:739–748.
6. Engel, J., M. Fechner, …, A. Stier. 1994. Anisotropic propagation of Ca^{2+} waves in isolated cardiomyocytes. *Biophys. J.* 66:1756–1762.
7. Cleveland, G. G., D. C. Chang, …, H. E. Rorschach. 1976. Nuclear magnetic resonance measurement of skeletal muscle: anisotropy of the diffusion coefficient of the intracellular water. *Biophys. J.* 16:1043–1053.
8. Alekseev, A., S. Reyes, and V. Selivanov. 2011. Compartmentation of membrane processes and nucleotide dynamics in diffusion-restricted cardiac cell microenvironment. *J. Mol. Cell Cardiol.* 52:401–409.
9. Shorten, P. R., and J. Sneyd. 2009. A mathematical analysis of obstructed diffusion within skeletal muscle. *Biophys. J.* 96:4764–4778.
10. Aliev, M. K. M., and A. N. A. Tikhonov. 2004. Random walk analysis of restricted metabolite diffusion in skeletal myofibril systems. *Mol. Cell. Biochem.* 256-257:257–266.
11. Vendelin, M., and R. Birkedal. 2008. Anisotropic diffusion of fluorescently labeled ATP in rat cardiomyocytes determined by raster image correlation spectroscopy. *Am. J. Physiol. Cell Physiol.* 295:C1302–C1315.
12. Liao, R., L. Nascimben, …, J. S. Ingwall. 1996. Decreased energy reserve in an animal model of dilated cardiomyopathy. Relationship to contractile performance. *Circ. Res.* 78:893–902.
13. Ingwall, J. S., and R. G. Weiss. 2004. Is the failing heart energy starved? On using chemical energy to support cardiac function. *Circ. Res.* 95:135–145.
14. Irving, T. C., J. Konhilas, …, P. P. de Tombe. 2000. Myofilament lattice spacing as a function of sarcomere length in isolated rat myocardium. *Am. J. Physiol. Heart Circ. Physiol.* 279:H2568–H2573.
15. Matsubara, I., and G. F. Elliott. 1972. X-ray diffraction studies on skinned single fibers of frog skeletal muscle. *J. Mol. Biol.* 72:657–669.
16. Woodhead, J. L., F.-Q. Zhao, …, R. Padrón. 2005. Atomic model of a myosin filament in the relaxed state. *Nature.* 436:1195–1199.
17. Zoghbi, M. E., J. L. Woodhead, …, R. Craig. 2008. Three-dimensional structure of vertebrate cardiac muscle myosin filaments. *Proc. Natl. Acad. Sci. USA.* 105:2386–2390.
18. Alamo, L., W. Wriggers, …, R. Padrón. 2008. Three-dimensional reconstruction of tarantula myosin filaments suggests how phosphorylation may regulate myosin activity. *J. Mol. Biol.* 384:780–797.
19. Kekenes-Huskey, P., A. Gillette, …, J. McCammon. 2012. Finite element estimation of protein-ligand association rates with post-encounter effects: applications to calcium binding in troponin C and SERCA. *Comput. Sci. Discov.* 5:014015.
20. Cheng, Y., P. Kekenes-Huskey, …, A. P. Michailova. 2012. Multi-scale continuum modeling of biological processes: from molecular electrodiffusion to sub-cellular signaling transduction. *Comput. Sci. Discov.* 5:015002.
21. Goel, P., J. Sneyd, and A. Friedman. 2006. Homogenization of the cell cytoplasm: the calcium bidomain equations. *Multiscale Model Simul.* 5:1045–1062.
22. Higgins, E. R., P. Goel, …, J. Sneyd. 2007. Modeling calcium microdomains using homogenization. *J. Theor. Biol.* 247:623–644.
23. Allaire, G. 1992. Homogenization and two-scale convergence. *SIAM J. Math. Anal.* 23:1482–1518.
24. Bourbatache, K., O. Millet, and A. Aït-Mokhtar. 2011. Multi-scale periodic homogenization of ionic transfer in cementitious materials. *In* Advances in Bifurcation and Degradation in Geomaterials, Springer Series in Geomechanics and Geoengineering. S. Bonelli, C. Dascalu, and F. Nicot, editors. Springer, New York, pp. 117–123.
25. Bensoussan, A., J. L. Lions, and G. Papanicolaou. 2011. Asymptotic Analysis for Periodic Structures. American Mathematical Society, Providence, RI.
26. Auriault, J. L., C. Boutin, and C. Geindreau. 2010. Homogenization of Coupled Phenomena in Heterogenous Media. ISTE/John Wiley & Sons, New York.
27. Auriault, J. L., and J. Lewandowska. 1997. Effective diffusion coefficient: from homogenization to experiment. *Transp. Porous Media.* 27:205–223.
28. Auriault, J., and J. Lewandowska. 1993. Homogenization analysis of diffusion and adsorption macrotransport in porous-media—macrotransport in the absence of advection. *Geotechnique.* 43:457–469.
29. Reference deleted in proof.
30. Geuzaine, C., and J.-F. Remacle. 2009. GMSH: a 3-D finite element mesh generator with built-in pre- and post-processing facilities. *Int. J. Numer. Methods Eng.* 79:1309–1331.
31. Tanner, B. C. W., T. L. Daniel, and M. Regnier. 2007. Sarcomere lattice geometry influences cooperative myosin binding in muscle. *PLOS Comput. Biol.* 3:e115.
32. Wu, S., J. Liu, …, K. A. Taylor. 2010. Electron tomography of cryofixed, isometrically contracting insect flight muscle reveals novel actin-myosin interactions. *PLoS ONE.* 5:e12643.
33. Behrmann, E. E., M. M. Müller, …, S. S. Raunser. 2012. Structure of the rigor actin-tropomyosin-myosin complex. *Cell.* 150:327–338.
34. Liao, T., Y. Zhang, …, J. McCammon. 2013. Multi-core CPU or GPU-accelerated multiscale modeling for biomolecular complexes. *Mol.-Based Math. Biol.* 1:164–179.
35. Logg, A., G. N. Wells, and J. Hake. 2012. DOLFIN: a C++/Python finite element library. *In* Automated Solution of Differential Equations by the Finite Element Method Springer, New York, pp. 173–225.
36. Vendelin, M., O. Kongas, and V. Saks. 2000. Regulation of mitochondrial respiration in heart cells analyzed by reaction-diffusion model of energy transfer. *Am. J. Physiol. Cell Physiol.* 278:C747–C764.
37. van Beek, J. H. G. M. 2007. Adenine nucleotide-creatine-phosphate module in myocardial metabolic system explains fast phase of dynamic regulation of oxidative phosphorylation. *Am. J. Physiol. Cell Physiol.* 293:C815–C829.

38. Kontrogianni-Konstantopoulos, A., M. A. Ackermann, …, R. J. Bloch. 2009. Muscle giants: molecular scaffolds in sarcomerogenesis. *Physiol. Rev.* 89:1217–1267.

39. Millman, B. M. 1998. The filament lattice of striated muscle. *Physiol. Rev.* 78:359–391.

40. ter Keurs, H. E. D. J. 2012. The interaction of Ca^{2+} with sarcomeric proteins: role in function and dysfunction of the heart. *Am. J. Physiol. Heart Circ. Physiol.* 302:H38–H50.

41. Sen, P. N., and P. J. Basser. 2005. A model for diffusion in white matter in the brain. *Biophys. J.* 89:2927–2938.

42. McGuffee, S. R., and A. H. Elcock. 2010. Diffusion, crowding and protein stability in a dynamic molecular model of the bacterial cytoplasm. *PLOS Comput. Biol.* 6:e1000694.

43. Długosz, M., and J. Trylska. 2011. Diffusion in crowded biological environments: applications of Brownian dynamics. *BMC Biophys.* 4:3.

44. O'Rourke, B., B. M. Ramza, and E. Marbán. 1994. Oscillations of membrane current and excitability driven by metabolic oscillations in heart cells. *Science.* 265:962–966.

45. Romashko, D. N., E. Marbán, and B. O'Rourke. 1998. Subcellular metabolic transients and mitochondrial redox waves in heart cells. *Proc. Natl. Acad. Sci. USA.* 95:1618–1623.

46. Wegmann, G., E. Zanolla, …, T. Wallimann. 1992. In situ compartmentation of creatine kinase in intact sarcomeric muscle: the acto-myosin overlap zone as a molecular sieve. *J. Muscle Res. Cell Motil.* 13:420–435.

47. Kinsey, S. T., and T. S. Moerland. 2002. Metabolite diffusion in giant muscle fibers of the spiny lobster *Panulirus argus*. *J. Exp. Biol.* 205:3377–3386.

48. Louch, W. E., O. M. Sejersted, and F. Swift. 2010. There goes the neighborhood: pathological alterations in T-tubule morphology and consequences for cardiomyocyte Ca^{2+} handling. *J. Biomed. Biotechnol.* 2010:503906.

49. Knowles, A. C., M. Irving, and Y.-B. Sun. 2012. Conformation of the troponin core complex in the thin filaments of skeletal muscle during relaxation and active contraction. *J. Mol. Biol.* 421:125–137.

50. Gordon, A. M. A., E. E. Homsher, and M. M. Regnier. 2000. Regulation of contraction in striated muscle. *Physiol. Rev.* 80:853–924.

51. Al-Khayat, H. A., R. W. Kensler, …, E. P. Morris. 2012. Atomic model of the human cardiac muscle myosin filament. *Proc. Natl. Acad. Sci. USA.* 110:318–323.

52. Nitsche, J. M., and G. Balgi. 1994. Hindered Brownian diffusion of spherical solutes within circular cylindrical pores. *Ind. Eng. Chem. Res.* 33:2242–2247.

53. Changsun, E., P. M. Kekenes-Huskey, and A. McCammon. 2013. Influence of neighboring reactive particles on diffusion-limited reactions. *J. Chem. Phys.* 139:044117.

54. Kinsey, S. T., B. R. Locke, …, T. S. Moerland. 1999. Diffusional anisotropy is induced by subcellular barriers in skeletal muscle. *NMR Biomed.* 12:1–7.

55. Cortassa, S., B. O'Rourke, …, M. A. Aon. 2009. Control and regulation of mitochondrial energetics in an integrated model of cardiomyocyte function. *Biophys. J.* 96:2466–2478.

56. Beard, D. A. 2005. A biophysical model of the mitochondrial respiratory system and oxidative phosphorylation. *PLOS Comput. Biol.* 1:e36.

57. Hake, J. J., A. G. A. Edwards, …, A. D. A. McCulloch. 2012. Modeling cardiac calcium sparks in a three-dimensional reconstruction of a calcium release unit. *J. Physiol.* 590:4403–4422.

58. Kekenes-Huskey, P. M., Y. Cheng, …, A. P. Michailova. 2012. Modeling effects of L-type Ca^{2+} current and Na^{+}-Ca^{2+} exchanger on Ca^{2+} trigger flux in rabbit myocytes with realistic T-tubule geometries. *Front Physiol.* 3:351.

59. Soeller, C., I. D. Jayasinghe, …, M. B. Cannell. 2009. Three-dimensional high-resolution imaging of cardiac proteins to construct models of intracellular Ca^{2+} signaling in rat ventricular myocytes. *Exp. Physiol.* 94:496–508.

60. Soeller, C., and M. B. Cannell. 1997. Numerical simulation of local calcium movements during L-type calcium channel gating in the cardiac dyad. *Biophys. J.* 73:97–111.

Molecular and Subcellular-Scale Modeling of Nucleotide Diffusion in the Cardiac Myofilament Lattice

Peter M. Kekenes-Huskey,[†]* Tao Liao,[‡] Andrew K. Gillette,[§] Johan E. Hake,[¶] Yongjie Zhang,[‡] Anushka P. Michailova,[‖] Andrew D. McCulloch,[‖] and J. Andrew McCammon[††]

[†]Department of Pharmacology, and [§]Department of Mathematics, University of California, San Diego, California; [¶]Simula School of Research and Innovation, Oslo, Norway; [‡]Department of Mechanical Engineering, Carnegie Mellon, Pittsburgh, Pennsylvania; and [‖]Department of Bioengineering, and [††]Howard Hughes Medical Institute, University of California, San Diego, California

Supporting Material

Homogenization

Mesh construction

Meshes were built for both the thin and thick filaments based on (34). For the thin filaments, a multi-level summation of Gaussian kernel functions was applied, for which there are three levels of resolution: atomic, residue, chain and domain. The density distribution of a single atom is represented using the Gaussian kernel function

$$G_{i_A}(\mathbf{x}) = e^{\kappa\left(\|\mathbf{x}-\mathbf{x}_{i_A}\|^2 - r_{i_A}^2\right)}, \tag{S1}$$

where κ is the decay rate, controlling the decay of the Gaussian kernel function. x_{i_A} and r_{i_A} are the center and radius of the i_A^{th} atom, respectively. The Gaussian density of the higher level structures are obtained through the summation of the lower levels:

$$G(\mathbf{x}) = \sum_{i_D}\left(\sum_{i_C}\left(\sum_{i_R}\left(\sum_{i_A} G_{i_A}(\mathbf{x})\right)^{P_R}\right)^{P_C}\right)^{P_D}, \tag{S2}$$

where i_D, i_C, i_R and i_A are the indices of the peptide, residue and atom, respectively. P_R, P_C and P_D are constant coefficients that control the local resolution of the model. By adjusting the parameters, the atomic level feature for the domain TnC and myosin heads are preserved, while the remainder of the thin filament surface is represented at lower resolution. This was accomplished using $P_R = 0.5$ and $P_C = 0.3$ for the low resolution (blurred) region; $P_R = 0.7$ and $P_C = 0.4$ was used for the high-resolution region (TnC and myosin heads). The thick filaments are modeled as simple cylinders. The filaments were assembled into a single Gaussian density map that was inserted into an outer cuboidal boundary. The dual contouring method was then adapted to adaptively generate a tetrahedral mesh from the density map. Quality improvement algorithms such as the face swapping, edge contraction and geometric flow were applied to improve the quality of the tetrahedra.

Validation of the homogenization approach.

To validate our implementation homogenization protocol, we apply the method to 1) a 'layered' problem for which analytical solutions of χ_i are available

(28) and 2) a lattice of parallel cylinders for which numerical estimates of D are provided (26). In 1), we consider a parallel array of impermeable slabs aligned along the x-axis, between which a particle may diffuse (see Fig 6. (28)). We seek χ_i satisfying (2) between the impermeable slabs, thus we created a 2D grid of dimensions 4.2 by 1.3 using Gmsh 2.7 (30). In Figure S3, we show the layered system consisting of a region of free diffusion (triangulated) between two impenetrable layers (gray). We solved (2) on this mesh assuming that the left and right boundaries were permeable (by enforcing periodicity through setting $\chi = 0$), while the top and bottom were impermeable (by enforcing the Neumann condition (2)) . In Figure S3 we plot χ_2 for the model geometry; the Neumann condition defined at the impermeable boundaries adjacent to the slabs (gray) yield a monotonically decreasing χ_2 function along increasing y. The analytical solutions to this problem (see Equations 87a-c in (28)) are given by

$$\chi_1 = \chi_1(x) \tag{S3}$$

$$\chi_2 = -y_2 + \chi_2(x) \tag{S4}$$

$$\chi_3 = \chi_3(x) \tag{S5}$$

We compare the analytical result for χ_2 with our predicted solution in Figure S3 and Figure S4 and find that the solutions are in exact agreement (within an arbitrary constant). Substitution of the $\nabla\chi_i$ into (3) yields the normalized effective diffusion constant, D, as $D = |\Omega_\epsilon|/|\Omega| \equiv \phi$, where ϕ is the accessible volume fraction, for i=1,3 (normal to the layered barriers) and $D = 0$ otherwise.

For 2), we compared the effective diffusivities predicted for cells representing a lattice of parallel cylinders. For the cylinder lattice, we created a unit cell with a circular obstacle of variable radius at its center, similar to Figure 6.14 of (26). In each 1x1x1 Å unit cell we embedded an impermeable cylinder whose radii varied from 0.1 to 0.4 Å, which yielded accessible volume fractions, ϕ, ranging from nearly 1.0 to 0.3. Similar to the layered problem, since the cylinder is invariant along the longitudinal axis, $\chi_z = 0$ and thus $D_L = \phi$, where D_L is the longitudinal component of the normalized effective diffusion constant. Since to our knowledge there are no analytical solutions for the transverse component of the effective diffusivity, D_T, we utilize the upper bound for the parallel cylinder lattice established by Hashin and Shtrikman (see Theory). Our predictions in Figure S5 are in agreement with the analytical value for D_L and the HS scaling relation for D_T. In agreement with intuition, D_T is smaller than D_L for $\phi \leq 1$. Moreover, we observe that the solutions for D_T nearly coincide with the upper

HS bound, as reported in Chapter 6 of (26) and are in agreement with the Maxwell-Garnett estimate reported in Eqn (23) of (41).

Error in homogenization estimates

Several factors could add variability to our estimates of the effective diffusion constants, including the relative arrangement and configuration of the thick and thin filaments, the resolution of the structures, as well as the resolution of the generated meshes. We demonstrated in the Results that the lattice arrangement and myosin head configuration influence D, and these estimates are considerably different from the case in which primitive representations of the filaments are assumed. To understand the variability arising from the mesh generation, we created several meshes at varying resolutions (from 140442 to 240353 vertices), to which we applied the homogenization protocol. We found that the mean D was (0.33, 0.35,0.45) with standard error (0.012,0.003,0.009 for n=4). Therefore, despite a nearly 50% reduction in the number of vertices, the standard error was less than 2%. We expect errors of similar magnitude for the remaining geometries; however, since it was not feasible to rebuild the geometries at several mesh resolutions, we did not provide estimates of the standard error in the reported tables. Nevertheless, based on the error from the most variable component, Dx, the 95% confidence interval is within +- 0.023 of the mean; hence all other means outside this interval are considered significant.

Reaction-Diffusion Model.

Model

The PDE is solved within a half-sarcomere geometry originally proposed in (36) and modified here (Figure S6). We define a region where the thin and thick filaments overlap within the A-band, adjacent to which is the I-band (the thin filaments anchoring region), and within the A-band is the H-zone where the thick filaments are anchored. The longitudinal ($\mathbf{x}$) axis of the sarcomere spans the Z and I zones (1.0 μm), myofibril and mitochondrion compartment are along the radial, or transverse, ($\mathbf{y}$ axis of the cell (1.2 μm), while the $\mathbf{z}$ axis is orthogonal to these axes. We assume the overlap region of the A-band, where ATPase activity occurs, spans x=0.2 to 0.8 and y = 0.0 to 1.0 per Vendelin et al (36). We assume the face at y=1.2 μmborders the inter-membrane space of the mitochondrion; along this boundary, ADP is exchanged with ATP according to the Van Beek model described below. All other boundaries are assumed to be reflective. Simulations were performed

for a 25x25x25 vertex, tetrahedralized mesh, for 1000 ms using time-steps of dt=10 ms and the parameters listed in Table S1. We assumed a piecewise linear continuous Galerkin basis set for the model, which was numerically solved using FEniCS (35). Time-dependence was introduced via the backward Euler approach and Newton's method was used to solve the resulting nonlinear problem.

For each time-step the mitochondrial ODE model provided an updated value of the nucleotide fluxes; the ODE model's estimates for $J_{hydrolysis}$ and J_{CK} were applied as source conditions in the PDE, whereas J_{diff} was applied as a boundary conditions. The ODE model was similarly updated with [ATP] and [ADP] predicted by the PDE model. The Van Beek ODE model was acquired from the CellML repository (http://www.cellML.org), pythonized via gotran (available at https://bitbucket.org/johanhake/gotran), and solved using the scipy function 'odeint' at 10,000 time points between the PDE time-intervals (dt=10ms). In Figure S7a we report the input time-dependent myosin ATPase rate ; all other states and fluxes are obtained by solving the ODE at each time step. The combined PDE and ODE model was analyzed for a 1000 ms time interval, following a 5 s equilibration period for the ODE model. To examine ADP gradients developed in absence of the CK pathway, we reduced the forward and backward rates of the CK equation by 98% as per (37). Details of our validation of the implementation are given in the Supporting Material. The code will be released at https://bitbucket.org/huskeypm/sarcomere.

Table S1: **Parameters**. *With exception to the listed quantities, all parameters for the Van Beek model are described in (37)*

Parameter	Value	Description
r_{ATP}	0.66	radius of ATP [nm]
D^{ϵ}_{ATP}	145	Bulk diffusion constant of ATP [μm^2/s] (36)
D^{ϵ}_{ADP}	145	Bulk diffusion constant of ADP [μm^2/s] (36)
$D_{reduced,i}$	0.1 $\cdot D_{bulk,i}$	Reduced diffusion constant of component i in muscle (Est)
$d_{card,MA}$	18.3	Cardiac myosin/actin distance [nm] (Est. from (14))
$d_{skel,MA}$	16.5	Skeletal myosin/actin distance [nm] (9)

Validation of Metabolism model

We validated our implementation in Figure S7, which shows that the average cytosolic nucleotide concentrations under two ATPase hydrolysis frequencies (135 and 220 BPM) are in sync with predictions given in Fig 2 of (37). In Figure 7(b), we show that ADP oscillations upon reduction of CK activity (VCK=0.02) in our model is in good agreement with Fig. 10 of (37). Because we did not explicitly rescale the amplitude of JATP for the VCK=0.02 case, the minimum ADP— concentration in our simulations (0.01 mM) are lower than the estimates in their figure (0.04). JCK/JATP and the diffusion fluxes estimated by the cellML code were passed to the finite element model as source and boundary conditions, respectively (Figure S9 for predicted values). Comparison of estimates from our finite element model Figure S8 with the cellML [ADP] predictions for vCK=1.0 and 0.02 demonstrate equivalent results.

Supplemental figures

Figure S1

Model lattice geometries a) Primitive unit cell for myofibril lattice. Thick (large diameter) and thin (small diameter) filament arrangement follows typical interfilament spacing in cardiac myofibrils. b) Unit cell akin to Shorten's geometry in Fig. 5 (9).

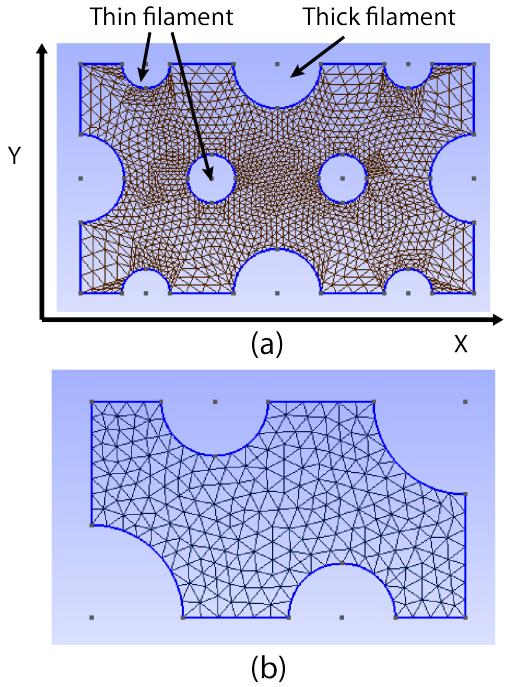

Figure S1:

Figure S2

Solutions of the homogenized diffusion equation χ_x satisfying Equation (2) based on the primitive myofibril unit cell (Figure S1) for diffusing particle diameters of 0 (a) and 6 nm (b). The thick filaments are represented by the large half-cylinders on the unit cell edges, while the thin filaments are interspersed along the cell edges and interior. Diffusional hindrance transverse to the myofibril lattice are evidenced by non-zero (red,blue) values of χ_x.

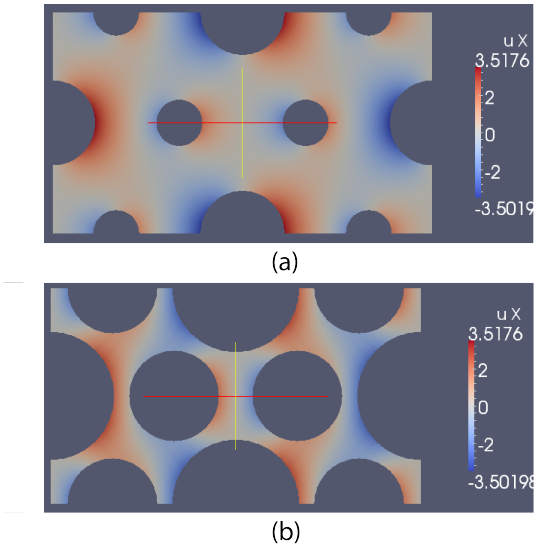

Figure S2:

Figure S3

Predicted χ_2 **solution for layered medium** . Predicted χ_2 field (aligned with the y-axis) for a layered slab. Substrate may freely diffuse along the x direction (left/right) but is impeded by the gray slabs along the y-direction.

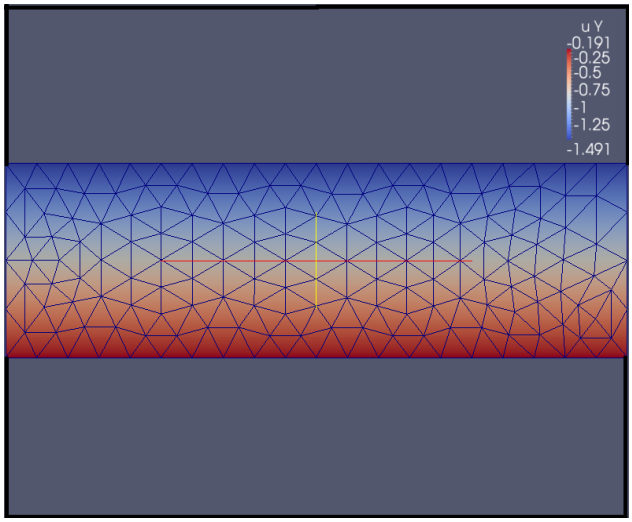

Figure S3:

Figure S4

Predicted χ_2 values for layered medium versus analytical solution Values of χ_2 extracted at x=0 from solution in Figure S4.

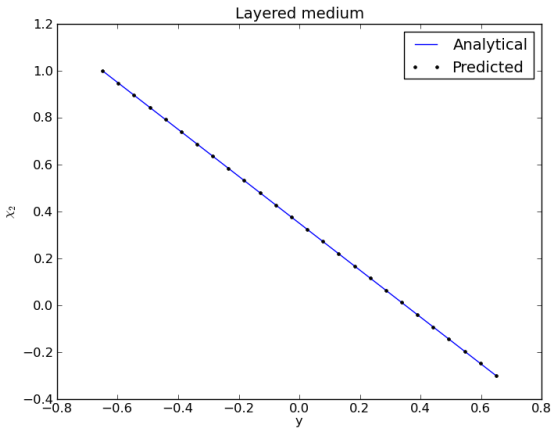

Figure S4:

Figure S5

Comparison of predicted effective diffusion constants for a lattice of parallel cylinders. Triangle and circle symbols correspond to our predictions D parallel, D_L, and transverse, D_T, to cylinders of increasing free volume, ϕ (and decreasing radius). The dashed line represents the analytical solution for D_L and upper bounds for D_T (26).

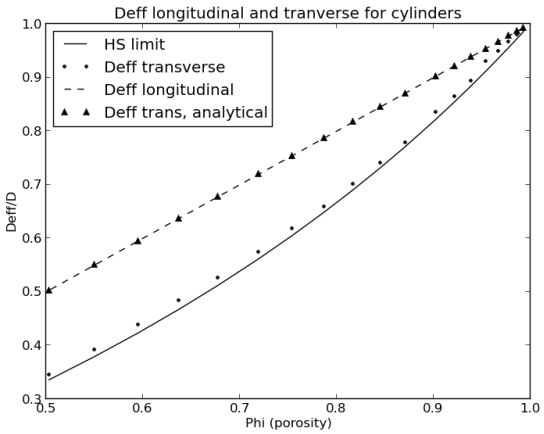

Figure S5:

Figure S6

Half-sarcomere model Half-sarcomere geometry based on Vendelin et al. (36). Region of thin and thick filament overlap designated as the A-band. Adjacent to the A-band are the I-band, which contains the Z-line, and at the A-band center is the H-zone, which contains the M-line. The longitudinal axis (x) of the sarcomere is 1.0 μm in length; the circumferential axis of the cell (y) is 1.2 μm in width. The **z** axis is aligned with the transverse direction of the cell. The overlap region of the A-band, where ATPase activity occurs, spans x=0.2 to 0.8 and y = 0.0 to 1.0 per Vendelin et al. (36). The face at y=1.2 μmborders the intermembrane space of the mitochondrium; along which ADP is exchanged with ATP via the diffusional fluxes $J_{diff,ATP}$ and $J_{diff,ADP}$. All other boundaries are assumed to be reflective.

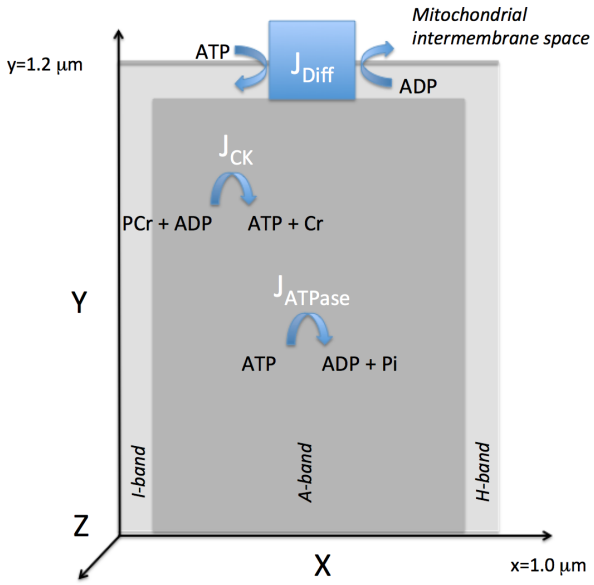

Figure S6:

Figure S7

Time course of the ATP hydrolysis flux a) JATP predicted by our implementation of Van Beek's cellML metabolism model (37) at 135 beats per minute (0-2 s) and 220 BPM (2-10 s) and applied to our finite element model. b) Validation of our implementation of the Van Beek code, in which the time course of ADP is presented under varying levels of creatine kinase activity (vCK=1.0 and 0.02, compare with Figure 10 of (37)) .

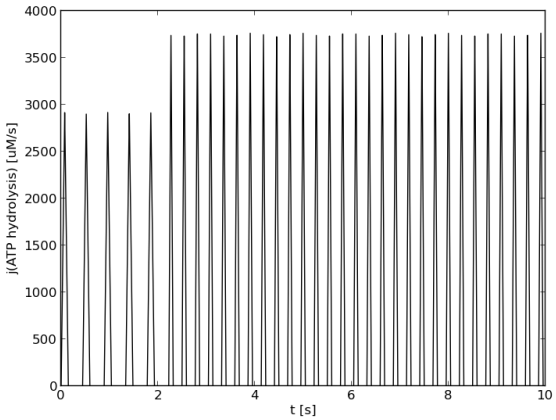
4000
3500
3000
2500
2000
1500
1000
500
0
j(ATP hydrolysis) [uM/s]
0
2
4
6
8
10
t [s]

(a)

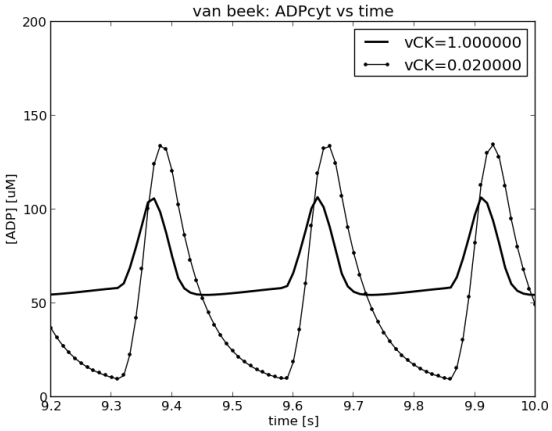
van beek: ADPcyt vs time
vCK=1.000000
vCK=0.020000
200
150
100
50
0
[ADP] [uM]
9.2
9.3
9.4
9.5
9.6
9.7
9.8
9.9
10.0
time [s]

(b)

Figure S7:

Figure S8

Predicted average ATP and ADP concentrations. Nucleotide concentrations predicted by the half-sarcomere finite element model over a 1 second interval using the anisotropic (Deff/D=[x,y,z], symbols) diffusion constant computed from the thin filament representation with three cross bridges, as well as the unhindered, isotropic diffusion constant (Deff/D=1.0, lines).

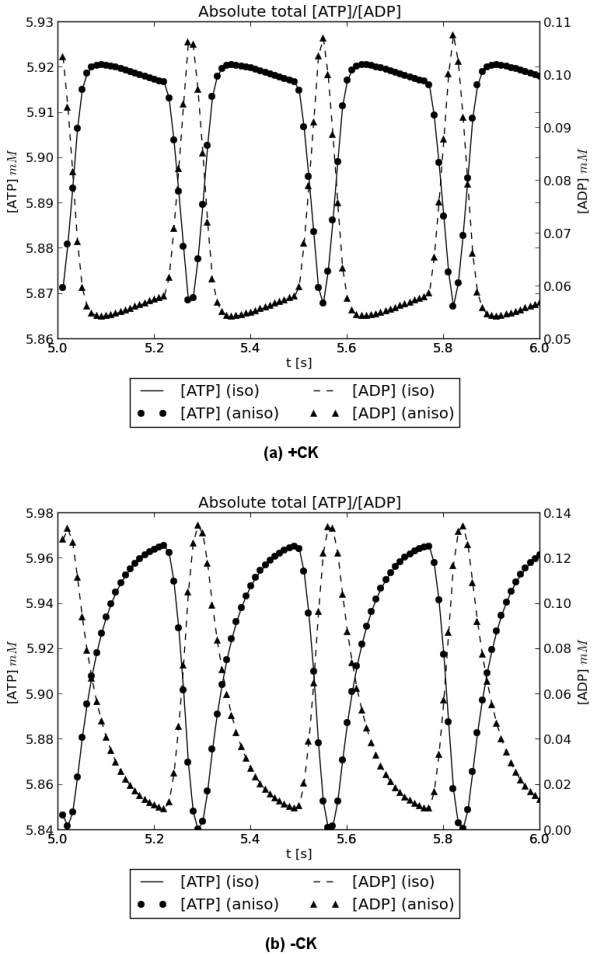

Figure S8:

Figure S9

Predicted average ATP hydrolysis and ATP diffusional fluxes from the PDE simulation. ATP fluxes originating from ATP hydrolysis (solid), the cytosolic creatine kinase reaction (dot dash) and the nucleotide exchange with the mitochondrion (dashed) are presented a) with CK and b) without CK activity.

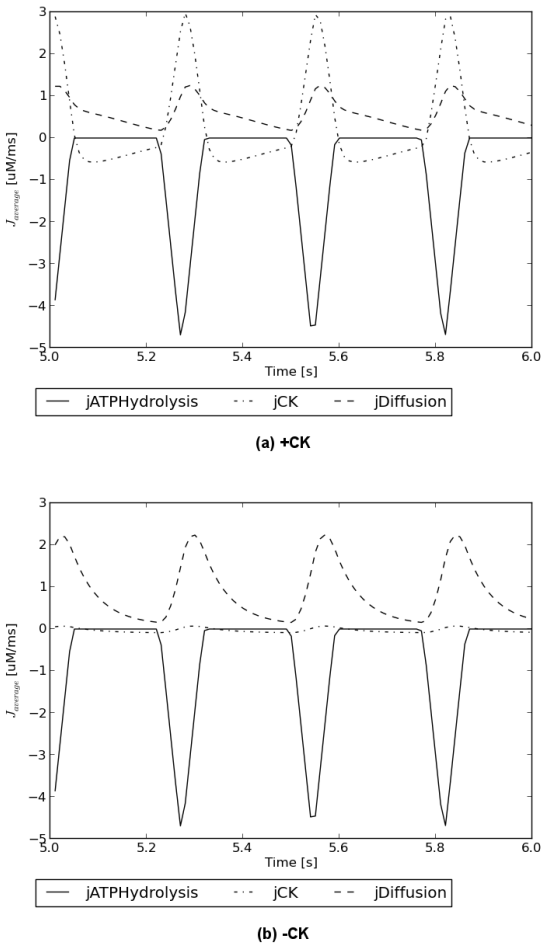

Figure S9:

Figure S10

Two-dimensional ADP concentrations. Reported at 5.3 s (corresponding to peak myosin ATPase activity) in the presence of CK (a,b) and in its absence (c,d), for the isotropic (a,c) and anisotropic (b,d) diffusion coefficients.

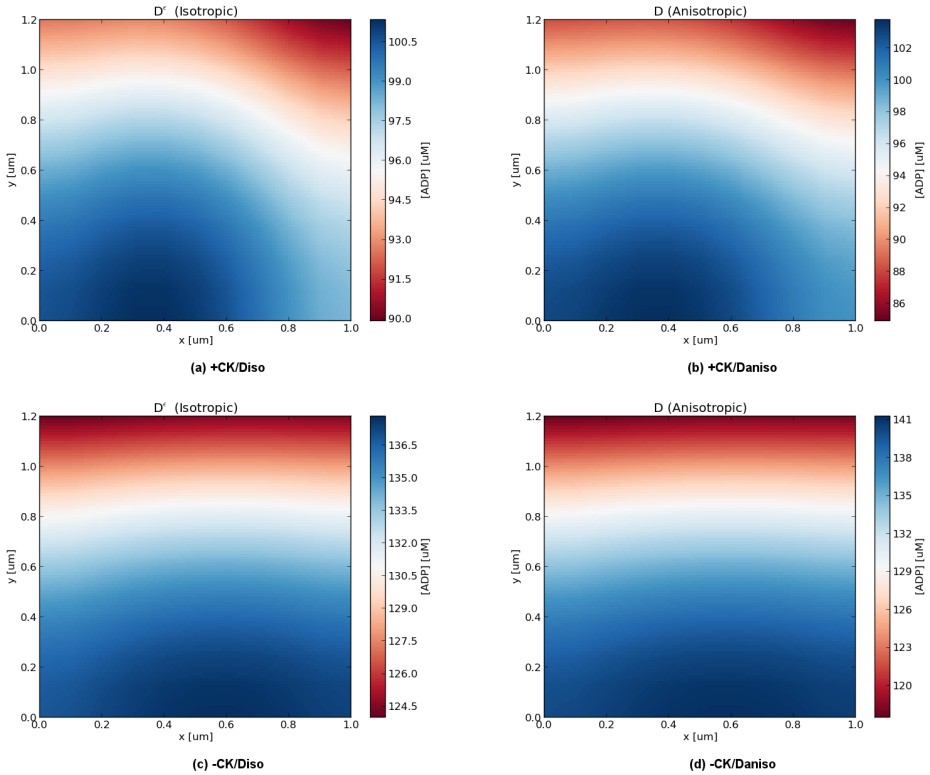

Figure S10:

Figure S11

Same as Figure S10, but with D reduced by ten-fold.

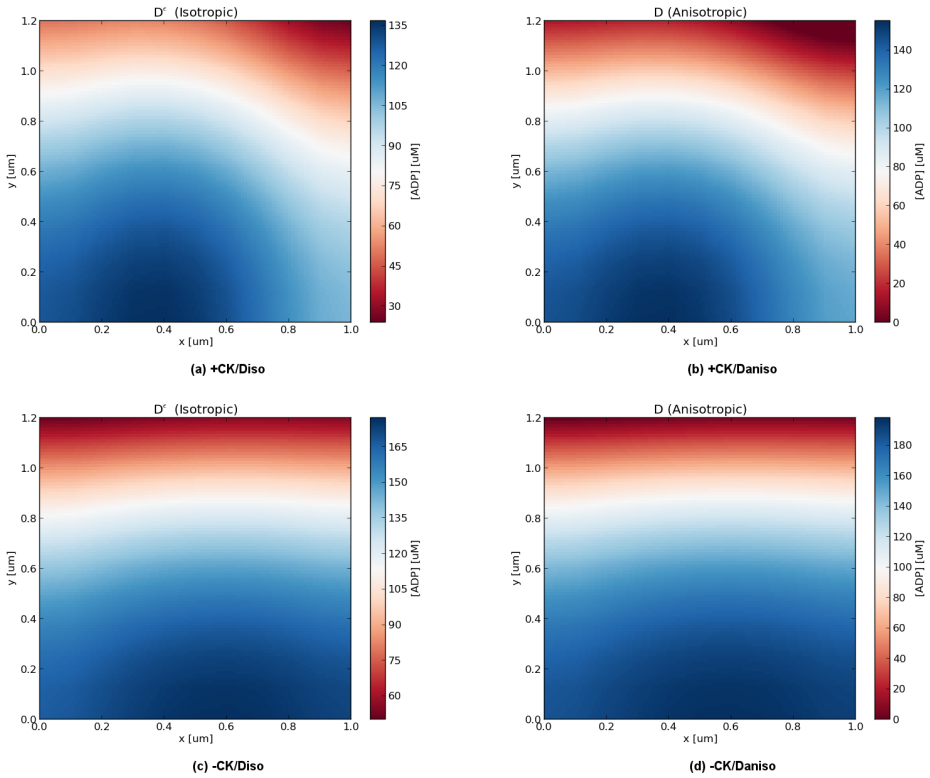
D^r (Isotropic)
D (Anisotropic)
y [um]
x [um]
[ADP] [uM]
(a) +CK/Diso
(b) +CK/Daniso
(c) -CK/Diso
(d) -CK/Daniso

Figure S11: